Magnetic Interactions of the Centrosymmetric Skyrmion Material math xmlns="http://www.w3.org/1998/Math/MathML" display="inline">mrow>msub>mrow>mi>Gd/mi>/mrow>mrow>mn>2/mn>/mrow>/msub>msub>mrow>mi>PdSi/mi>/mrow>mrow>mn>3/mn>/mrow>/msub>/mrow>/math>

Joseph A. M. Paddison, Binod K. Rai, Andrew F. May, Stuart Calder, Matthew B. Stone, Matthias D. Frontzek, and Andrew D. Christianson

Phys. Rev. Lett. **129**, 137202 — Published 23 September 2022

DOI: 10.1103/PhysRevLett.129.137202

Magnetic Interactions of the Centrosymmetric Skyrmion Material Gd_2PdSi_3

Joseph A. M. Paddison,[1,*] Binod K. Rai,[1,2] Andrew F. May,[1] Stuart A. Calder,[3]
Matthew B. Stone,[3] Matthias D. Frontzek,[3] and Andrew D. Christianson[1,†]

[1]*Materials Science and Technology Division, Oak Ridge National Laboratory, Oak Ridge, TN 37831, USA*
[2]*Savannah River National Laboratory, Aiken, South Carolina, 29808, USA*
[3]*Neutron Scattering Division, Oak Ridge National Laboratory, Oak Ridge, Tennessee 37831, USA*

The experimental realization of magnetic skyrmion crystals in centrosymmetric materials has been driven by theoretical understanding of how a delicate balance of anisotropy and frustration can stabilize topological spin structures in applied magnetic fields. Recently, the centrosymmetric material Gd_2PdSi_3 was shown to host a field-induced skyrmion crystal, but the skyrmion stabilization mechanism remains unclear. Here, we employ neutron-scattering measurements on an isotopically-enriched polycrystalline Gd_2PdSi_3 sample to quantify the interactions that drive skyrmion formation. Our analysis reveals spatially-extended interactions in triangular planes, and large ferromagnetic inter-planar magnetic interactions that are modulated by the Pd/Si superstructure. The skyrmion crystal emerges from a zero-field helical magnetic order with magnetic moments perpendicular to the magnetic propagation vector, indicating that the magnetic dipolar interaction plays a significant role. Our experimental results establish an interaction space that can promote skyrmion formation, facilitating identification and design of centrosymmetric skyrmion materials.

Magnetic skyrmions are topologically-nontrivial spin textures with potentially transformative applications in quantum computing and information storage [1–3]. Skyrmion crystals usually occur in noncentrosymmetric magnets, in which they can be stabilized by antisymmetric exchange interactions [4, 5]. However, it was recently shown that skyrmion crystals can be stabilized in centrosymmetric systems by frustrated (competing) interactions [6, 7], presenting the exciting prospects of higher skyrmion densities and manipulation of chiral degrees of freedom by external fields [8, 9]. While a small number of candidate centrosymmetric skyrmion materials have been identified [10–13], experimentally determining the magnetic interactions driving this behavior remains a key challenge. Addressing this challenge is a prerequisite for designing and manipulating skyrmion-based devices.

The hexagonal material Gd_2PdSi_3 provides a rare example of a skyrmion crystal in a centrosymmetric system [10]. In Gd_2PdSi_3, triangular layers of magnetic Gd^{3+} ions are separated by honeycomb $PdSi_3$ layers [Fig. 1(a)] [14]. A transition from the paramagnetic state occurs at $T_N = 21$ K to an incommensurate magnetic order with propagation vector $\mathbf{q} = [q00]^*$ with $q \approx 0.14$ [10]. The observed $\mathbf{q}$ may be stabilized by competition between ferromagnetic nearest-neighbor interactions and antiferromagnetic further-neighbor interactions [Fig. 1(a,b)] [6, 7]. Application of a magnetic field below T_N yields a giant topological Hall effect, signifying a transition to a topologically-nontrivial skyrmion crystal, which is a triple-$\mathbf{q}$ structure formed by superposing magnetic helices with $\mathbf{q} = [q00]^*$, $[0q0]^*$, and $[\bar{q}q0]^*$ [10]. The bulk magnetic susceptibility follows a Curie-Weiss law with spin $S = 7/2$, $g = 2$, and a ferromagnetic Weiss temperature $\theta \approx 30$ K, suggesting that Gd^{3+} ions possess spin-only local moments [15–17]. However, coupled electronic and spin correlations develop well above T_N, as indicated by a minimum in the resistivity at $\sim 2T_N$ and a large negative magnetoresistance that persists up to $\sim 3T_N$ [16–18].

To explain spin textures in centrosymmetric systems such as Gd_2PdSi_3, it is crucial to understand the system's underlying magnetic interactions. The experimental observation of Fermi surface nesting with a wavevector similar to $\mathbf{q}$ suggests the relevance of long-ranged RKKY interactions [26], while a theoretical study indicates that local exchange processes are also important [27]. However, quantifying the interactions experimentally is a complex problem, for three main reasons. First, the ordered magnetic structure in zero applied field is not conclusively solved [10, 17, 28]. Second, although the crystal structure may be approximately described with a statistical distribution of Pd and Si, these atoms actually form

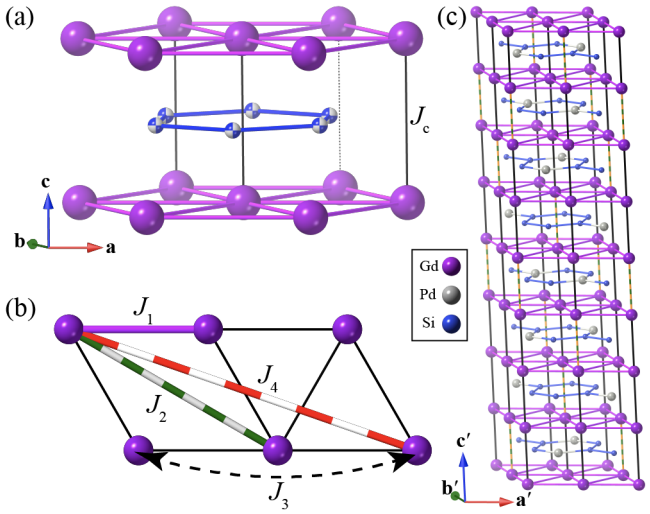

Figure 1. (a) Parent crystal structure of Gd_2PdSi_3 (space group $P6/mmm$; $a \approx 4.06$ Å, $c \approx 4.09$ Å [19]). (b) Magnetic interactions within triangular Gd^{3+} layers. (c) Proposed low-symmetry Pd/Si superstructure showing ...ABCDBADC... stacking of $PdSi_3$ layers ($a' = b' = 2a$, $c' = 8c$). The highest-symmetry space group compatible with the superlattice ordering is $Fddd$ [19]. Black lines show inter-layer bonds with two Pd and four Si neighbors, and striped orange/green lines show inter-layer bonds with six Si neighbors.

a superlattice that may affect exchange processes [Fig. 1(c)] [14]. Third, the large neutron-absorption cross-section of isotopically-natural Gd makes neutron-scattering experiments on large single crystals challenging. So far, this has prevented the use of neutron-scattering experiments to understand the magnetic interactions of Gd_2PdSi_3.

Here, we employ neutron-scattering experiments on $^{160}Gd_2PdSi_3$ to obtain a model of its zero-field magnetic structure and interactions that explains multiple experimental observations. We obtain the following key results. First, magnetic interactions within triangular layers are spatially extended and of competing sign. Second, ferromagnetic interactions between layers are dominant, and strongly modulated by the Pd/Si superlattice. Third, below T_N, a helix with the spin plane perpendicular to $\mathbf{q}$ is the only structure consistent with our neutron data and physical constraints, suggesting the magnetic dipolar interaction plays a significant role below T_N [29]. Finally, we confirm that our interaction model explains the skyrmion crystal at small applied magnetic fields below T_N [10, 30]. Our results provide a foundation for theoretical modeling and experimental manipulation of spin textures in Gd_2PdSi_3.

We prepared a polycrystalline sample of $^{160}Gd_2PdSi_3$ (mass ∼0.8 g) by arc melting. Arc-melted samples were wrapped in Ta foil, sealed in a quartz tube under a vacuum, and annealed at 800 C for one week. The sample quality was confirmed by bulk magnetometry and by powder X-ray diffraction, which reveals broad superlattice peaks consistent with 126(6) Å domains of the superstructure shown in Fig. 1(c) [19]. To minimize neutron absorption, the sample was 98.1% enriched with ^{160}Gd, and an annular sample geometry was used for neutron diffraction and spectroscopy experiments, which were performed using the HB-2A and SEQUOIA instruments at ORNL, respectively.

Figure 2(a) shows magnetic diffuse-scattering data $I(Q)$ collected above T_N using HB-2A ($\lambda = 2.4067$ Å). The data are background-subtracted and placed in absolute intensity units by normalization to the nuclear Bragg scattering. As the sample is cooled below 40 K, $I(Q)$ increases at small wavevectors, $Q \lesssim 0.3$ Å^{-1}, indicating the development of predominantly ferromagnetic short-range correlations. Figure 2(b) shows that the bulk magnetic susceptibility χT exhibits a large upturn over the same temperature range, as expected because $\chi T \propto I(\mathbf{Q} = \mathbf{0})$ at high temperature [31]. For RKKY interactions with Fermi wave-vector k_F, theory predicts an increase in $I(Q \lesssim 2k_F)$ as T_N is approached from above, with a simultaneous upturn in the resistivity [32]. To test this prediction, Fig. 2(c) compares $I(Q \to 0)$—obtained from χT and by averaging $I(Q)$ over $0.1 \le Q \le 0.3$ Å^{-1}—with published resistivity measurements [16]. Both $I(Q \to 0)$ and the resistivity shown an upturn at the same temperature (∼40 K), in qualitative agreement with the RKKY prediction [32]. This result suggests that RKKY interactions may play a significant role in Gd_2PdSi_3.

We quantify the magnetic interactions by analyzing $I(Q)$

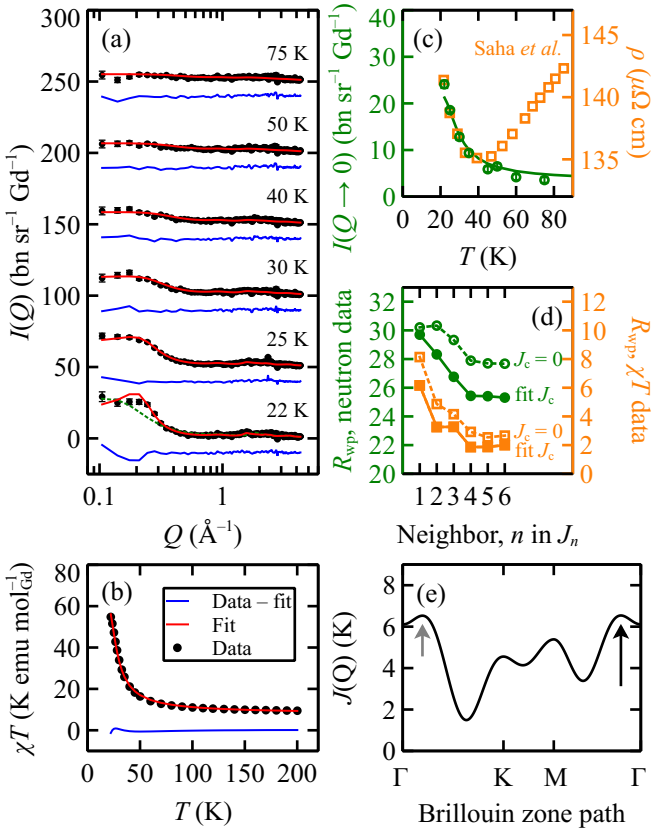

Figure 2. (a) Magnetic diffuse scattering above T_N, showing experimental data (black circles), model fits (red lines), and data – fit (blue lines). Successive curves are shifted vertically by 50 bn sr^{-1} Gd^{-1}. Data collected and fitted at 35 K, 45 K, and 60 K follow the same trends and are omitted for clarity. The dotted green line shows the 22 K fit with five intra-layer couplings and $J_c = 0$. (b) Bulk magnetic susceptibility data and fit (colors as above). (c) Comparison of $I(Q \to 0)$ from neutron data (green circles) and magnetic susceptibility data (solid green line) with published resistivity data from Ref. 16 (orange squares). (d) Dependence of goodness-of-fit metric R_{wp} for neutron data (green circles) and susceptibility data (orange squares) on the number of intra-layer neighbors, n. Solid symbols show results when inter-layer coupling J_c was fitted, and open symbols show results for $J_c = 0$. (e) Dependence of $J(\mathbf{Q})$ along high-symmetry paths ($\Gamma = (000)$; K $= (\frac{1}{3}\frac{1}{3}0)$; M $= (\frac{1}{2}00)$). Positions of global and local maxima in $J(\mathbf{Q})$ are shown by long black and short gray arrows, respectively.

and χT data measured at $T > T_N$ within a Heisenberg model,

$$H_{ex} = -\frac{1}{2}\sum_{i,j} J_{ij}\mathbf{S}_i \cdot \mathbf{S}_j, \qquad (1)$$

where $\mathbf{S}_i$ denotes a classical spin vector with position $\mathbf{R}_i$ and length $\sqrt{S(S+1)}$, and the interaction parameters $J_{ij} \in \{J_1, J_2, J_3, J_4, J_c\}$ are shown in Fig. 1(a,b). We make two simplifying assumptions in this high-temperature analysis. First, we neglect non-Heisenberg terms such as the magnetic dipolar interaction and single-ion anisotropy, which have negligible effect above T_N because of their small energy scales [19]. Second, we assume the high-symmetry hexagonal structure,

J_c (K)	J_1 (K)	J_2 (K)	J_3 (K)	J_4 (K)
1.97(46)	0.31(9)	0.19(15)	0.27(18)	−0.21(5)

Table I. Fitted values of magnetic interaction parameters. Parameter uncertainties indicate 3σ confidence intervals.

neglecting a possible variation in J_{ij} due to the Pd/Si superstructure. To calculate $I(Q)$ from the J_{ij}, we apply reaction-field theory, a self-consistent mean-field theory that gives good agreement with classical Monte Carlo simulations [33–35]. Within reaction-field theory, the wavevector-dependent susceptibility $\chi(\mathbf{Q}) = \chi_0/\{1-\chi_0[J(\mathbf{Q})-\lambda]\}$ [36], where $J(\mathbf{Q}) = \sum_j J_{ij}\exp(i\mathbf{Q}\cdot\mathbf{R}_j)$, $\chi_0 = S(S+1)/3$, λ is obtained self-consistently by enforcing that $\int_{BZ}\chi(\mathbf{Q})d\mathbf{Q} = S(S+1)$ [36], and $I(Q)$ is calculated by spherically averaging $I(\mathbf{Q}) = cT[f(Q)]^2\chi(\mathbf{Q})$, where $c = 0.1937$ bn [31] and $f(Q)$ is the Gd^{3+} magnetic form factor [37].

We first tested a two-dimensional model by setting $J_c = 0$ and refining the intra-layer couplings $\{J_1,...,J_n\}$ to our $I(Q)$ and χT data shown in Fig. 2(a) and (b). This model does not represent the data well. By contrast, also refining the inter-layer coupling J_c substantially improves the refinement quality metric R_{wp} [Fig. 2(d)], demonstrating that the interactions are three-dimensional. To estimate the spatial extent of the interactions, Fig. 2(d) shows the dependence of R_{wp} on the number of J_n fitted in addition to J_c. No significant improvement is obtained for $n > 4$; hence, our minimal model contains $\{J_1,J_2,J_3,J_4,J_c\}$. The optimal parameter values from a global fit to $I(Q)$ and χT data are given in Table I. Including dipolar interactions does not significantly affect the refined J_{ij} [19]. Ferromagnetic J_c is dominant, while intra-layer interactions compete between antiferromagnetic J_4 and shorter-range ferromagnetic couplings, resembling an RKKY interaction [38, 39]. Figure 2(e) shows the corresponding $J(\mathbf{Q})$, which is maximal at the calculated propagation vector, $\mathbf{q}_{calc} \approx [0.12,0,0]^*$. Notably, the energy scale $S(S+1)J(\mathbf{q}_{calc})$ is similar to first-principles results [27, 40]. While $\mathbf{q}_{calc}$ is smaller than the measured low-temperature $\mathbf{q} \approx [0.14,0,0]^*$, the difference is plausible because $\mathbf{q}$ decreases with increasing temperature below T_N [10]. Interestingly, a local $J(\mathbf{Q})$ maximum occurs along the $[110]^*$ direction with $< 0.2\%$ energy difference from $J(\mathbf{q}_{calc})$. Fermi-surface measurements of Gd_2PdSi_3 show a nesting wavevector $\sim [\frac{1}{6}\frac{1}{6}0]^*$ [26], while Tb_2PdSi_3 exhibits short-range magnetic ordering with this periodicity [41], suggesting quasi-degeneracy may be generic to these materials. Finally, we considered an alternative five-parameter model containing two inter-layer and three intra-layer couplings. While this model yields a comparable refinement of $I(Q)$ and χT measurements, it does not agree well with inelastic neutron-scattering data [19].

We now investigate the zero-field magnetic structure for $T < T_N$. Taking the hexagonal structure as the parent phase, there are three magnetic irreducible representations (irreps) that correspond, respectively, to sinusoidal modulations of the Gd ordered magnetic moment μ_{ord} along orthogonal directions $\mathbf{a}^*$, $\mathbf{b}$, and $\mathbf{c}$ [Fig. 3(a)] [42]. Alternatively, combining pairs of irreps yields helices with μ_{ord} in the ab, a^*c, or bc plane [Fig. 3(b)]. Helical and sinusoidal models have been proposed for the zero-field structure of Gd_2PdSi_3 [27, 28]. A triple-$\mathbf{q}$ meron-antimeron structure was also proposed [10]. In Fig. 3(c), we compare the Rietveld refinement for each model with the magnetic diffraction pattern, obtained as the difference between the 1.5 K and 25 K data. All magnetic Bragg peaks are explained by Gd magnetic ordering, indicating that any Pd magnetic polarization is below the detection limit of our data. For each model, Fig. 3(e) shows R_{wp}, and Fig. 3(f)

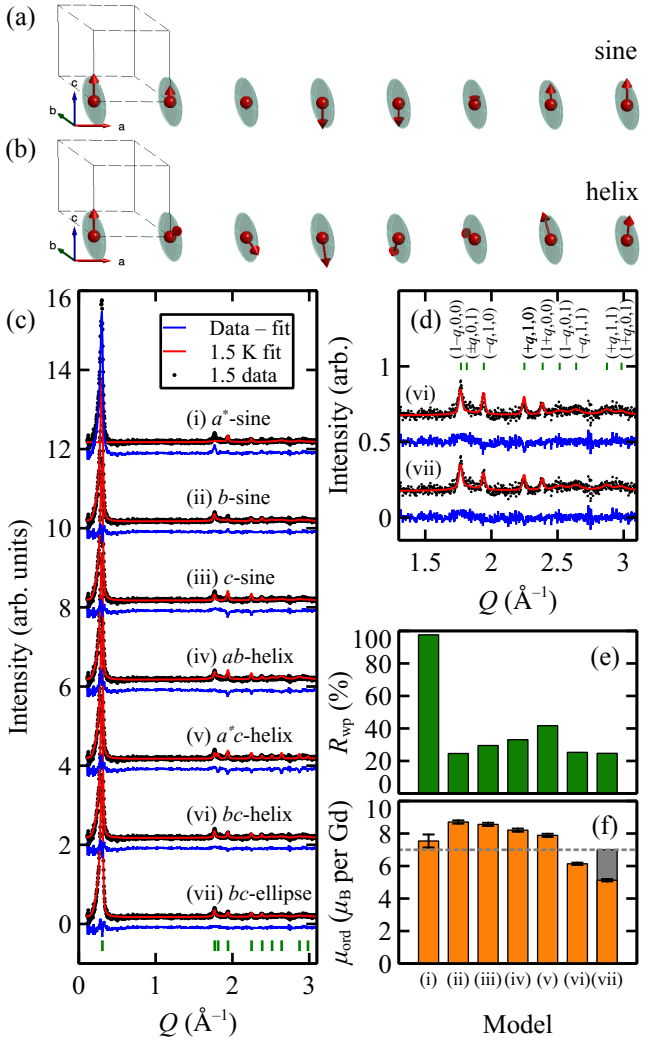

Figure 3. (a) Sinusoidal spin-density wave with spin axis perpendicular to $\mathbf{q}$. (b) "Proper screw" helix with spin plane perpendicular to $\mathbf{q}$. (c) Magnetic diffraction data at 1.5 K (black circles), model fits (red lines), and data – fit (blue lines). (d) Magnetic diffraction data, fits and data – fit (colors as above) on an expanded Q-axis scale for models (vi) and (vii), showing broadening of peaks with $l \neq 0$ and improved fit for the elliptical helix (vii) compared to the circular helix (vi). (e) Goodness-of-fit metric R_{wp} for each model. (f) Maximum refined value of the ordered magnetic moment μ_{ord} per Gd^{3+} for each model. Parameter uncertainties represent 1σ confidence intervals. For model (vii), $\mu_{ord} \parallel \mathbf{b}$ is shown as a gray bar.

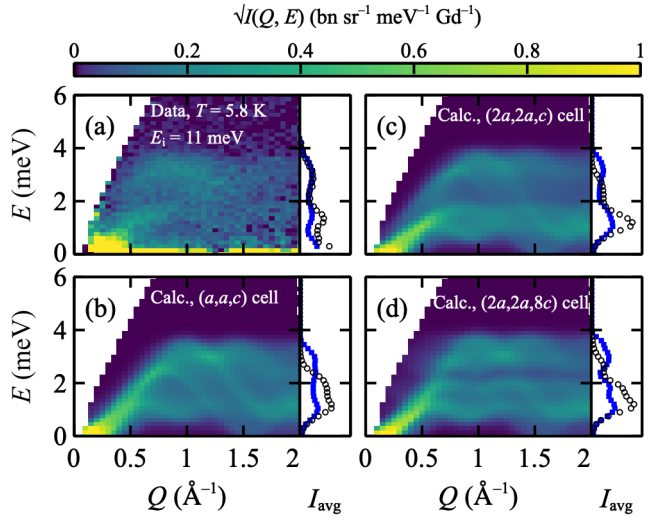

Figure 4. (a) Inelastic neutron-scattering data measured at $T = 5.8$ K with $E_i = 11$ meV. Data are corrected for detailed balance and diffuse scattering is subtracted. (b) Linear spin-wave theory (LSWT) calculation for the interaction parameters given in Table I. (c) LSWT calculation with J_c split by $\Delta = 0.8$ (defined in the text) for Pd/Si superlattice ordering with periodicity $(2a, 2a, c)$. (d) LSWT calculation with J_c split by $\Delta = 0.8$ for Pd/Si superlattice ordering with periodicity $(2a, 2a, 8c)$. Each panel contains a color plot (left) of $\sqrt{I(Q,E)}$, and line cuts of intensity $I_{\rm avg}$ averaged over $0.5 < Q < 0.7$ Å^{-1} (black circles) and $0.5 < Q < 2.0$ Å^{-1} (blue squares).

shows the refined maximum value of $\mu_{\rm ord}$. The $\mathbf{a}^*$-sine model (i), with spins $\mathbf{S} \parallel \mathbf{q}$, would give zero intensity for the strong $(q00)$ magnetic peak, and so is ruled out. Of the remaining models, **b**-sine (ii), *bc*-helix (vi), and *bc*-ellipse (vii) structures yield similarly high-quality refinements. The meron-antimeron structure has an identical diffraction pattern to its single-**q** analog, the *bc*-helix, and is not shown separately. The refined $\mu_{\rm ord}$ is a key discriminating factor, as any physical model must satisfy the constraint that $\max(\mu_{\rm ord}) \leq 2S\mu_{\rm B}$ $(= 7.0\mu_{\rm B}$ for $Gd^{3+})$ to ensure consistency with magnetic susceptibility and saturation magnetization measurements. This constraint rules out the **b**-sine model with $\max(\mu_{\rm ord}) = 8.7\mu_{\rm B}$ [Fig. 3(f)]. It also disfavors the meron-antimeron structure, for which $\max(\mu_{\rm ord}) = \frac{3}{2}\mu_{\rm ord}^{\rm helix}$, where $\mu_{\rm ord}^{\rm helix} = 6.14(7)\,\mu_{\rm B}$ is the refined ordered moment of the *bc*-helix. Thus, the key result of our Rietveld analysis is that only "proper screw" helices with $\mathbf{S} \perp \mathbf{q}$, models (vi) and (vii), yield good fits and reasonable $\mu_{\rm ord}$ values. The best such refinement is for an elliptical helix with $\mu_{\parallel \mathbf{c}} = 5.13(7)\,\mu_{\rm B}$, and $\mu_{\parallel \mathbf{b}}$ fixed to $7.0\,\mu_{\rm B}$. Notably, the ordered moment is not fully polarized as $\mu_{\rm ord}^{\rm helix} < 2S\mu_{\rm B}$ at 1.5 K. Magnetic peaks are also selectively broadened compared to nuclear peaks [Fig. 3(d)]. Refinement of a quadratic-in-l size-broadening term yields magnetic domain dimensions of 332(8) Å in the *ab*-plane *vs.* 27(2) Å along **c**, which may be a consequence of the disordered stacking of $PdSi_3$ layers indicated by our X-ray diffraction data [14, 19].

The magnetic excitation spectrum at $T \ll T_{\rm N}$ provides a sensitive test of our model. Our inelastic neutron-scattering data ($E_i = 11$ meV) show spin-wave excitations at $T = 5$ K, superimposed on a diffuse magnetic background that likely occurs because $\mu_{\rm ord}^{\rm helix} < 2S\mu_{\rm B}$. In Fig. 4(a), we show $I'_{5\,\rm K} = I_{5\,\rm K} - [1 - (\mu_{\rm ord}^{\rm helix}/2S\mu_{\rm B})^2]I_{25\,\rm K}$, which isolates the spin-wave contribution. Our data show an overall bandwidth of approximately 4 meV. For $E < 4$ meV, the spectrum has a broad energy dependence with intensity minima for $0 \lesssim E \lesssim 1$ meV and $2 \lesssim E \lesssim 3$ meV that are most apparent at small $Q \lesssim 0.7$ Å^{-1}. Figure 4(b) shows the calculated spectrum for the interaction parameters given in Table I and a single-**q** helical ground state, calculated within linear spin-wave theory [43] using the SpinW program [44]. Including the dipolar interaction has only a small effect on the spectrum [19]. This model reproduces the overall bandwidth, but fails to explain the intensity minimum for $2 \lesssim E \lesssim 3$ meV. Attempts to refine $\{J_1, J_2, J_3, J_4, J_c\}$ to the inelastic data also failed to reproduce this feature. To explain our data, it was necessary to consider the effect of the Pd/Si superstructure on J_c. All proposed models of the Pd/Si superstructure involve doubling the unit cell along **a** and **b**, such that 75% of J_c bonds (notated J_{c+}) have four Si and two Pd neighbors, while the remaining J_c bonds (notated J_{c-}) have six Si neighbors [Fig. 1(c)]. We assume the superstructure splits J_c by an amount ΔJ_c, such that $J_{c+} = J_c(1 + \Delta/4)$ and $J_{c-} = J_c(1 - 3\Delta/4)$, and neglect any splitting of the weaker interactions. For the $(2a, 2a, 8c)$ superstructure shown in Fig. 1(c), the stacking of $J_{c\pm}$ bonds is ...ABCDBADC... [14], whereas the $(2a, 2a, c)$ superstructure considered in Ref. 27 has ...AAA... stacking. Taking $\Delta = 0.8$ with the $(2a, 2a, c)$ superstructure reproduces the intensity minimum for $2 \lesssim E \lesssim 3$ meV and yields good overall agreement with our inelastic neutron-scattering data [Fig. 4(c)], without degrading the agreement with $I(Q)$ data above $T_{\rm N}$ [19]. Taking $\Delta = 0.8$ with the $(2a, 2a, 8c)$ superstructure also generates intensity minima, but yields worse agreement with our data [Fig. 4(d)]. Our results show that the Pd/Si superstructure strongly enhances J_c for bonds with Pd neighbors, perhaps consistent with a superexchange contribution here.

We use extensive Monte Carlo simulations [45] to calculate the phase diagram of our model as a function of temperature T and applied magnetic field $\mathbf{B} \parallel \mathbf{c}$. The spin Hamiltonian is given by

$$H = H_{\rm ex} + g\mu_{\rm B}B\sum_i S_i^z + D\sum_{i>j} \frac{\mathbf{S}_i \cdot \mathbf{S}_j - 3\,(\mathbf{S}_i \cdot \hat{\mathbf{r}}_{ij})\,(\mathbf{S}_j \cdot \hat{\mathbf{r}}_{ij})}{(r_{ij}/r_1)^3}, \tag{2}$$

where, to stabilize helical ordering with $\mathbf{S} \perp \mathbf{q}$, we include the magnetic dipolar interaction with magnitude $D = 0.037$ K at the nearest-neighbor distance r_1 [29, 46]. To minimize finite-size effects, we constrain the interactions to stabilize $\mathbf{q}_{\rm MC} = [q_{\rm MC}00]^* \approx \mathbf{q}_{\rm calc}$, with commensurate $q_{\rm MC} = \frac{1}{8}$ or $\frac{1}{9}$. The calculated magnetic susceptibility $\chi_{zz}^{\rm calc}(B,T)$ is shown in Fig. 5(a), and reveals both similarities and differences with experiment [30, 47]. In agreement with experiment, we find $T_{\rm N}^{\rm calc} \approx 20$ K, and below $T_{\rm N}$, a transition from a helical to a skyrmion crystal at small B (calculated as 0.25 T; c.f. 0.38 T

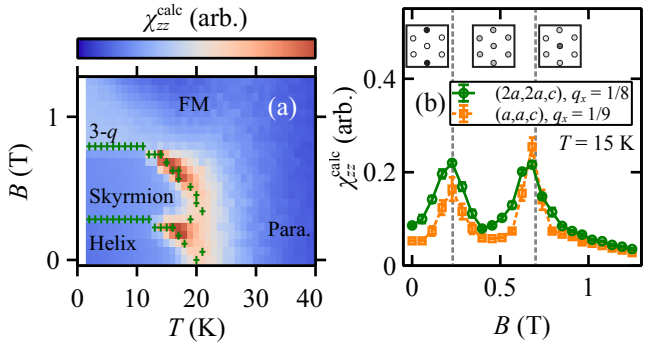

Figure 5. (a) Calculated magnetic susceptibility $\chi_{zz}^{\rm calc}$ and estimated phase boundaries (green crosses) for our interaction model, obtained using Monte Carlo simulations. Results are shown for $q_{\rm MC} = \frac{1}{9}$ and a $9\times9\times9$ supercell of the hexagonal unit cell. (b) Calculated $\chi_{zz}^{\rm calc}$ at $T = 15$ K for the distorted $(2a, 2a, c)$ supercell with $\Delta = 0.8$ and $q_{\rm MC} = \frac{1}{8}$ (green circles), and the undistorted structure with $\Delta = 0$ and $q_{\rm MC} = \frac{1}{9}$ (orange squares). The calculated magnetic diffraction patterns are for each phase are shown above, for $B = 0.11$, 0.40, and 0.79 T (left to right). The values of B are scaled by the quantum correction factor $\sqrt{(S+1)/S} \approx 1.134$.

experimentally [30]). At larger B, a further transition occurs to a topologically-trivial triple-**q** phase previously identified using mean-field theory [29]. The single-**q** *vs.* triple-**q** nature of each phase is revealed by its calculated magnetic diffraction pattern [insets in Fig. 5(b)]. The behavior is not qualitatively affected by the splitting of J_c, or by the precise value of $q_{\rm MC}$ [Fig. 5(b)]. Given the simplicity of our model, its reasonable agreement with experiment at small B is satisfying; however, it does not explain the large increase in saturation field on cooling the sample ($B_{\rm sat} \approx 8$ T at 2 K [30]) or the presence of magnetic transitions for $B > 1$ T [47]. These differences motivate further theoretical work to understand the role of non-Heisenberg interactions.

Our neutron-scattering results provide an experimental understanding of the magnetic interactions in Gd_2PdSi_3 and clarify its zero-field magnetic structure. This approach may provide insight into other centrosymmetric skyrmion materials, such as $Gd_3Ru_4Al_{12}$ and $GdRu_2Si_2$ [11, 13]. Notably, our interaction model explains key aspects of the experimental behavior without invoking biquadratic or multi-spin interactions [48]. However, the spin dynamics can only be understood by accounting for the Pd/Si superstructure, suggesting it is important to include this in models. We anticipate that this model of the skyrmion stabilization mechanism in Gd_2PdSi_3 will facilitate design and identification of new centrosymmetric skyrmion hosts, including in materials where large single-crystal samples are unavailable or unsuitable for neutron-scattering measurements.

We are grateful to Cristian Batista, Matthew Cliffe, Randy Fishman, Shang Gao, and Stephen Nagler for valuable discussions. This work was supported by the U.S. Department of Energy, Office of Science, Basic Energy Sciences, Materials Sciences and Engineering Division. This research used resources at the High Flux Isotope Reactor and Spallation Neutron Source, DOE Office of Science User Facilities operated by the Oak Ridge National Laboratory. The isotope used in this research was supplied by the U.S. Department of Energy Isotope Program, managed by the Office of Isotope R&D and Production.

* paddisonja@ornl.gov
† christiansad@ornl.gov

[1] Y. Tokura, N. Kanazawa, *Chem. Rev.* **121**, 2857 (2021).
[2] A. Fert, N. Reyren, V. Cros, *Nat. Rev. Mater.* **2**, 17031 (2017).
[3] A. N. Bogdanov, C. Panagopoulos, *Nat. Rev. Phys.* **2**, 492 (2020).
[4] S. Mühlbauer, *et al.*, *Science* **323**, 915 (2009).
[5] X. Z. Yu, *et al.*, *Nature* **465**, 901 (2010).
[6] T. Okubo, S. Chung, H. Kawamura, *Phys. Rev. Lett.* **108**, 017206 (2012).
[7] A. O. Leonov, M. Mostovoy, *Nat. Commun.* **6**, 8275 (2015).
[8] X. Yu, *et al.*, *Proc. Nat. Acad. Sci.* **109**, 8856 (2012).
[9] X. Yao, J. Chen, S. Dong, *New J. Phys.* **22**, 083032 (2020).
[10] T. Kurumaji, *et al.*, *Science* **365**, 914 (2019).
[11] M. Hirschberger, *et al.*, *Nat. Commun.* **10**, 5831 (2019).
[12] S. Gao, *et al.*, *Nature* **586**, 37 (2020).
[13] N. D. Khanh, *et al.*, *Nat. Nanotechnol.* **15**, 444 (2020).
[14] F. Tang, *et al.*, *Phys. Rev. B* **84**, 104105 (2011).
[15] P. Kotsanidis, J. Yakinthos, E. Gamari-Seale, *J. Magn. Magn. Mater.* **87**, 199 (1990).
[16] S. R. Saha, *et al.*, *Phys. Rev. B* **60**, 12162 (1999).
[17] H. Zhang, *et al.*, *New J. Phys.* **22**, 083056 (2020).
[18] R. Mallik, E. V. Sampathkumaran, M. Strecker, G. Wortmann, *Europhys. Lett. (EPL)* **41**, 315 (1998).
[19] See supplemental material for supplemental figures, tables of refinement results, experimental and computational methods, and Refs. 20-25.
[20] F. James, M. Roos, *Comp. Phys. Commun.* **10**, 343 (1975).
[21] F. James, *MINUIT Function Minimization and Error Analysis: Reference Manual Version 94.1*, CERN (1994).
[22] T. Proffen, T. R. Welberry, *Acta Crystallogr. A* **53**, 202 (1997).
[23] M. Enjalran, M. J. P. Gingras, *Phys. Rev. B* **70**, 174426 (2004).
[24] Z. Wang, C. Holm, *J. Chem. Phys.* **115**, 6351 (2001).
[25] I. A. Blech, B. L. Averbach, *Physics* **1**, 31 (1964).
[26] D. S. Inosov, *et al.*, *Phys. Rev. Lett.* **102**, 046401 (2009).
[27] T. Nomoto, T. Koretsune, R. Arita, *Phys. Rev. Lett.* **125**, 117204 (2020).
[28] S. H. Moody, *et al.*, *arXiv* 2010.14326 (2021).
[29] O. I. Utesov, *Phys. Rev. B* **105**, 054435 (2022).
[30] M. Hirschberger, *et al.*, *Phys. Rev. B* **101**, 220401 (2020).
[31] S. W. Lovesey, *Theory of Neutron Scattering from Condensed Matter: Polarization Effects and Magnetic Scattering*, vol. 2 (Oxford University Press, Oxford, 1987).
[32] Z. Wang, K. Barros, G.-W. Chern, D. L. Maslov, C. D. Batista, *Phys. Rev. Lett.* **117**, 206601 (2016).
[33] D. Hohlwein, J.-U. Hoffmann, R. Schneider, *Phys. Rev. B* **68**, 140408 (2003).
[34] P. H. Conlon, J. T. Chalker, *Phys. Rev. B* **81**, 224413 (2010).
[35] G. Pokharel, *et al.*, *Phys. Rev. Lett.* **125**, 167201 (2020).
[36] D. E. Logan, Y. H. Szczech, M. A. Tusch, *Europhys. Lett. (EPL)* **30**, 307 (1995).
[37] P. J. Brown, *International Tables for Crystallography* (Kluwer Academic Publishers, Dordrecht, 2004), vol. C, chap. Magnetic

Form Factors, pp. 454–460.
[38] Z. Wang, Y. Su, S.-Z. Lin, C. D. Batista, *Phys. Rev. Lett.* **124**, 207201 (2020).
[39] Z. Wang, C. D. Batista, *arXiv* 2111.13976 (2021).
[40] J. Bouaziz, E. Mendive-Tapia, S. Blügel, J. B. Staunton, *Phys. Rev. Lett.* **128**, 157206 (2022).
[41] M. Frontzek, *et al.*, *J. Phys.: Condens. Matter* **19**, 145276 (2007).
[42] A. Wills, *J. Phys. IV France* **11**, 133 (2001).
[43] R. S. Fishman, J. A. Fernandez-Baca, T. Rõõm, *Spin-Wave Theory and its Applications to Neutron Scattering and THz Spectroscopy*, 2053-2571 (Morgan and Claypool Publishers, 2018).
[44] S. Toth, B. Lake, *J. Phys.: Condens. Matter* **27**, 166002 (2015).
[45] M. E. J. Newman, G. T. Barkema, *Monte Carlo Methods in Statistical Physics* (Oxford University Press, Oxford, 1999).
[46] O. I. Utesov, *Phys. Rev. B* **103**, 064414 (2021).
[47] S. Spachmann, A. Elghandour, M. Frontzek, W. Löser, R. Klingeler, *Phys. Rev. B* **103**, 184424 (2021).
[48] S. Hayami, Y. Motome, *Phys. Rev. B* **103**, 024439 (2021).